INTERNATIONAL JOURNAL FOR NUMERICAL METHODS IN ENGINEERING
Int. J. Numer. Meth. Engng 2005; **64**:940–972
Published online 23 August 2005 in Wiley InterScience (www.interscience.wiley.com). DOI: 10.1002/nme.1401

Three-dimensional immersed finite element methods for electric field simulation in composite materials

R. Kafafy[1], T. Lin[2,*,†], Y. Lin[3,4] and J. Wang[1]

[1]*Department of Aerospace and Ocean Engineering, Virginia Polytechnic Institute and State University, 520 McBryde Hall, Blacksburg, VA 24061, U.S.A.*
[2]*Department of Mathematics, Virginia Polytechnic Institute and State University, 520 McBryde Hall, Blacksburg, VA 24061, U.S.A.*
[3]*Department of Mathematical Sciences, University of Alberta, Edmonton, Alberta, Canada T6G 2G1*
[4]*Northeastern University at Qinhuangdao, Qinhuangdao, Hebei 066044, P. R. China*

SUMMARY

This paper presents two immersed finite element (IFE) methods for solving the elliptic interface problem arising from electric field simulation in composite materials. The meshes used in these IFE methods can be independent of the interface geometry and position; therefore, if desired, a structured mesh such as a Cartesian mesh can be used in an IFE method to simulate 3-D electric field in a domain with non-trivial interfaces separating different materials. Numerical examples are provided to demonstrate that the accuracies of these IFE methods are comparable to the standard linear finite element method with unstructured body-fit mesh. Copyright © 2005 John Wiley & Sons, Ltd.

KEY WORDS: immersed finite elements; elliptic boundary value problems; discontinuous coefficients; Cartesian meshes

1. INTRODUCTION

This paper presents a class of finite element (FE) methods that can use structured Cartesian mesh to compute the electric field in a three-dimensional domain with interfaces separating different media materials. For the simplicity of presentation, we assume that the solution domain $\Omega \subset \mathbb{R}^3$ is a convex polygonal domain, the interface Γ is a surface separating Ω into two sub-domains Ω^-, Ω^+ such that $\Omega = \Omega^- \cup \Omega^+ \cup \Gamma$, see the sketch in Figure 1. The media property

*Correspondence to: T. Lin, Department of Mathematics, Virginia Polytechnic Institute and State University, 520 McBryde Hall, Blacksburg, VA 24061, U.S.A.
†E-mail: tlin@math.vt.edu

Contract/grant sponsor: NSF; contract/grant number: CMF-0427951
Contract/grant sponsor: NSERC

Received 28 June 2004
Revised 8 November 2004
Accepted 11 May 2005

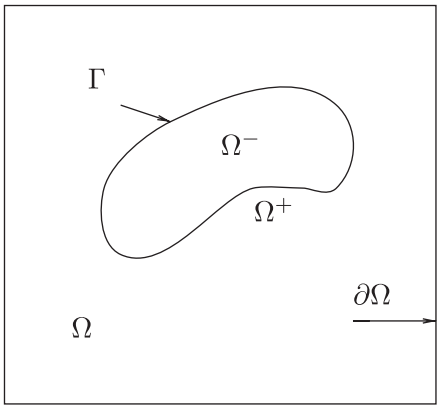

Figure 1. A sketch of the domain for the interface problem.

is described by a material-dependent coefficient $\beta(\mathbf{x})$ (i.e. permittivity) such that

$$\beta(x, y, z) = \begin{cases} \beta^-, & \mathbf{x} \in \Omega^- \\ \beta^+, & \mathbf{x} \in \Omega^+ \end{cases}$$

The electric field $\Phi(\mathbf{x})$ is assumed to be described by following interface problem of the 3-D Poisson's equation in Ω:

$$-\nabla \cdot (\beta \nabla \Phi) = f, \quad \mathbf{x} = (x, y, z) \in \Omega \subset \mathbb{R}^3 \tag{1}$$

$$\Phi|_{\partial\Omega_D} = g_D \tag{2}$$

$$\beta \frac{\partial \Phi}{\partial n}\bigg|_{\partial\Omega_N} = g_N \tag{3}$$

together with the jump conditions on the interface surface Γ:

$$[\Phi]|_\Gamma = 0 \tag{4}$$

$$[\beta \Phi_n]|_\Gamma = 0 \tag{5}$$

The primary motivation for developing this class of methods is for applications in plasma simulations using particle-in-cell (PIC) codes [1, 2]. A PIC code models a plasma as many macro-particles and follows the evolution of the orbits of individual particles in the self-consistent electromagnetic field. While originally developed as research tools to study kinetic phenomena in plasmas, PIC codes are increasingly being used in recent years as engineering tools for such applications as plasma processing, electric propulsion, spacecraft environmental interactions, etc. For engineering applications, a PIC code often needs to be sophisticated enough so complex geometric and field effects associated with the device surface can be modelled properly and yet computationally efficient enough so large-scale particle simulations

can be performed routinely within a reasonable time period. However, accuracy and computing speed often represent conflicting requirements for a PIC code.

Many existing numerical methods based on either the FE [3, 4] or the finite difference approach [5, 6] can be applied to solve the electric field accurately in the presence of a complex boundary. However, these conventional methods are not always suitable for use in PIC codes. In a PIC code, the particles are located anywhere the simulation domain but the field quantities are defined only on discrete mesh points. A PIC code uses a 'gather' step to interpolate fields from mesh points to particle positions to push particles and a 'scatter' step to deposit particle quantities to mesh points for solving the electric field. The particle trajectories and the electric fields are solved iteratively between a field solver and a particle pusher. Since a PIC code typically spends a significant portion of its computing time performing these two particle-mesh interpolation steps and pushing particles, most PIC codes use structured, Cartesian grids. In a standard Cartesian mesh PIC code, the location of memory of quantities defined in neighbouring cells can be found trivially via indexing. This is in contrast to a tetrahedral cell-based or unstructured grid-based PIC code, where the neighbours of a given cell must be found by lookups in a table or other methods requiring additional memory references, and a fairly complex scheme is typically needed to determine a particle's new cell [7]. As a result, a tetrahedral cell-based or unstructured mesh-based particle code can be significantly more expensive computationally than a standard orthogonal mesh PIC code for large-scale simulations [8]. On the other hand, a finite difference method-based field solver using structured (such as rectangular) meshes are susceptible of losing accuracy in the fields in the vicinity of a irregular boundary.

Due to the conflicting requirements from an accurate field solver and a speedy particle pusher, the plasma–material interface represents a major challenge in the application of PIC codes for device modelling. All current particle simulation codes use standard finite difference or FE methods to solve the electric field. These conventional methods are not sufficient for large-scale problems involving complex object boundaries in the simulation domain.

The objective of this study is to develop a new field solver using structured Cartesian meshes that is capable of resolving the electric fields accurately in a domain with complex boundary/interface geometry. The recently developed immersed finite element (IFE) method [9–13] provides a promising approach to develop such a field solver. We note that the IFE method discussed in this article is different from the one in Reference [14] where a different idea is used to solve different types of differential equations, even though these two methods coincidentally share the same name.

The essential idea in the IFE methods is that their mesh can be formed without consideration of the interface location. Hence, instead of using the unstructured mesh to body-fit the optics surface, an IFE method can use efficient structured Cartesian meshes to resolve the electric field in a domain with complicated boundary/interface geometries. Naturally, elements in the mesh of an IFE method can be classified into (1) interface elements whose interiors are cut through by the interface, and (2) non-interface elements. We note that if a mesh is fine enough, most of the elements are non-interface elements. Interface elements are far fewer, and are in the vicinity of the interface. The usual FE basis functions can be used in non-interface elements to handle the approximation. However, similar to those methods based on the finite difference immersed/imbeded boundary techniques, see References [15, 16] and references therein, an IFE method has to handle interface elements with special attentions or the method will lose accuracy in the vicinity of the interface where important physics usually happens. Our specific task here

is to develop IFE basis functions in interface elements that can incorporate the interface jump conditions *required by the physics* in a way such that the overall accuracy of the resulting IFE methods is maintained. Another advantage of the IFE methods over other methods such as meshless method is that the structured Cartesian mesh provides a very natural and efficient particle locating mechanism for a PIC code.

The IFE methods fall into the general frame of using specially designed (instead of generic) FE functions for a particular problem [17, 18]. Exemplary methods within this frame are the partition of unity method and the extended finite element methods (X-FEMs) [19–21]. X-FEMs are very versatile and they can be used to handle many problems with discontinuity including the interface problem considered here. The central idea of an X-FEM is to employ appropriate enrichment functions at the places necessary. Both the enrichment functions and the usual shape functions defined at the nodes of a mesh are used. The resulting algebraic system consists of more unknowns than that based on shape functions defined at the nodes. In contrast, the IFE method employs modified shape functions at the places necessary, but no extra unknowns are introduced in the solution domain. Consequently, the resulting algebraic system consists of exactly the same number of unknowns as that based on shape functions defined at the nodes, and even the structure (such as sparsity structure of involved matrices) of the algebraic system are preserved. In addition, each unknown in the IFE method has a clear physical meaning and this is a preferable feature for many applications such as the PIC simulation.

This article is organized as follows: Section 2 develops the axis-symmetric IFE method. Section 3 presents the IFE method for the general 3-D interface problem. Section 4 presents numerical examples for demonstrating the approximation capability of the IFE methods. Section 5 contains summary and conclusions.

2. AN AXIS-SYMMETRICAL IFE METHOD

This section presents the IFE method for calculating the electric field $\Phi(\mathbf{x})$ in a convex polygonal axis-symmetrical composite domain $\Omega \subset \mathbb{R}^3$ which is assumed to be formed by rotating a convex polygonal 2-D domain $\tilde{\Omega} = \{(z, r) \mid r \geqslant 0\} \subset \mathbb{R}^2$ around the z-axis. We assume that $\tilde{\Omega}$ is separated into two sub-domains $\tilde{\Omega}^+$ and $\tilde{\Omega}^-$ by a curve $\tilde{\Gamma}$ whose rotation around the z-axis forms the interface Γ in Ω. Using the cylindrical transformation

$$x = r\cos(\theta), \quad y = r\sin(\theta), \quad z = z$$

we can reduce the BVP (1)–(3) to the following BVP of $\tilde{\Phi}(z, r) = \Phi(\mathbf{x})$:

$$-\frac{\partial}{\partial r}\left(r\beta\frac{\partial\tilde{\Phi}}{\partial r}\right) - \frac{\partial}{\partial z}\left(r\beta\frac{\partial\tilde{\Phi}}{\partial z}\right) = rf, \quad (r, z) \in \tilde{\Omega} \tag{6}$$

$$\tilde{\Phi}|_{\partial\tilde{\Omega}_D} = g_D \tag{7}$$

$$r\beta\frac{\partial\tilde{\Phi}}{\partial n}\bigg|_{\partial\tilde{\Omega}_N} = g_N \tag{8}$$

Similarly, the interface jump conditions of Φ on Γ can be reduced to the interface jump conditions of $\tilde{\Phi}$ at $\tilde{\Gamma}$ as follows:

$$[\tilde{\Phi}]|_{\tilde{\Gamma}} = 0 \tag{9}$$

$$\left[r\beta \frac{\partial \tilde{\Phi}}{\partial n} \right]\Bigg|_{\tilde{\Gamma}} = 0 \tag{10}$$

with

$$\beta(z, r) = \begin{cases} \beta^-, & (z, r) \in \tilde{\Omega}^- \\ \beta^+, & (z, r) \in \tilde{\Omega}^+ \end{cases}$$

We first discuss the IFE space suitable for solving the above axis-symmetrical interface problem. As usual, to solve an interface problem by FE method, we start from a mesh $\mathscr{T}_h$ of $\tilde{\Omega}$. Even though the boundary value problem involves a solution domain $\tilde{\Omega}$ that consists of two materials separated by an interface curve $\tilde{\Gamma}$, we ignore the interface and introduce a mesh $\mathscr{T}_h$, which can be structured if necessary, just according to the geometry of the solution domain $\tilde{\Omega}$. Certainly, the mesh should retain the usual FE partition qualities. For example, the mesh should be fine enough according to the geometry of the interface curve and the physics involved. If the solution domain $\tilde{\Omega}$ is a rectangle, then a Cartesian mesh might be a preferred choice for many applications.

For the simplicity of presentation, we consider a triangular mesh $\mathscr{T}_h$. A quadrilateral mesh can also be used similarly [13]. Since the mesh formed in $\tilde{\Omega}$ is independent of the interface $\tilde{\Gamma}$, some of the elements in the mesh will intersect with $\tilde{\Gamma}$, and the rest do not. We will call an element a non-interface element if it does not intersect with the interface or if the interface passes through two of its vertices; otherwise, we will call this element an interface element. We note that, when a mesh is fine enough most of its elements are non-interface elements because $\tilde{\Gamma}$ is a 1-D object and only those elements in the vicinity of $\tilde{\Gamma}$ have the possibility to become interface elements.

As usual, the basic construction of an IFE space can be carried out through each element of the mesh. First, for a non-interface element $T \in \mathscr{T}_h$, because T contains only one material, we can just use the standard linear local nodal FE basis functions to handle the approximation there. It is known that there are three linear local nodal FE basis functions in T, and we use $S_h(T)$ to denote the space spanned by these functions.

Then, for a typical interface element $T \in \mathscr{T}_h$, we use $A_1 = (z_1, r_1)^{\mathrm{T}}$, $A_1 = (z_2, r_2)^{\mathrm{T}}$, $A_3 = (z_3, r_3)^{\mathrm{T}}$ to denote its vertices, and use $D = (z_D, r_D)^{\mathrm{T}}$ and $E = (z_E, r_E)^{\mathrm{T}}$ to denote the points where the interface $\tilde{\Gamma}$ intersects the edges of this element, see the sketch in Figure 2. Since the interface $\tilde{\Gamma}$ separates T into two sub-sets T^- and T^+, we naturally try to form a piecewise FE function by two first degree polynomials defined in T^- and T^+, respectively. The key idea is to make sure that the FE function satisfies the jump conditions (9) and (10) across the interface. Note that each polynomial of degree one has three freedoms (coefficients). The values of a FE function specified at the vertices of T provide three restrictions. The flux jump condition (10) on $\overline{DE}$ provides another. We can have two more restrictions by imposing the jump condition (9) at the interface points D and E. Intuitively, these six conditions can yield

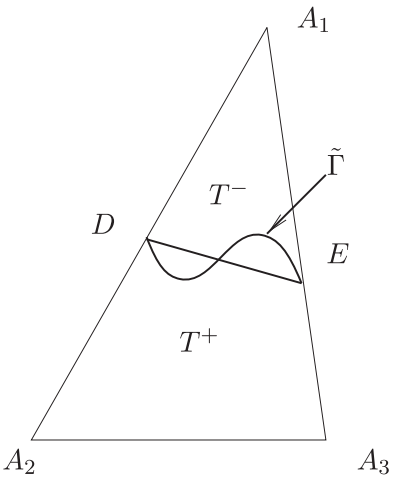

Figure 2. A typical interface triangle $\Delta A_1A_2A_3$. The curve between D and E is part of the interface $\tilde{\Gamma}$.

the desired piecewise linear polynomial in an interface element. In summary, we construct the local nodal basis functions in an interface element as follows:

$$\phi(z,r)=\begin{cases}\phi^-(z,r)=a_1r+b_1z+c_1, & (z,r)\in T^-\\ \phi^+(z,r)=a_2r+b_2z+c_2, & (z,r)\in T^+\\ \phi^-(D)=\phi^+(D), \quad \phi^-(E)=\phi^+(E) & \\ r\beta^-\nabla\phi^-\cdot\mathbf{n}(\overline{DE})-r\beta^+\nabla\phi^+\cdot\mathbf{n}(\overline{DE})=0 & \end{cases} \tag{11}$$

where $\mathbf{n}(\overline{DE})$ is the unit vector perpendicular to the line $\overline{DE}$.

We note that the r factor can be eliminated from the last equation of (11). Therefore, the local nodal basis functions we want to construct for the 3-D axis-symmetrical interface problem are the same as those developed for the general 2-D interface problems in References [11, 12]. Theorem 2.1 of Reference [11] indicates that for $i=1,2,3$, there exists a unique local nodal function $\phi_i(r,z)$ defined by (11) such that

$$\phi_i(A_j)=\begin{cases}1 & \text{when } i=j\\ 0 & \text{when } i\neq j\end{cases}$$

Then, we form the local FE space $S_h(T)$ in T as the linear space spanned by these local nodal basis functions $\phi_i, i=1,2,3$.

Finally, following the standard procedure, see Reference [11] for example, we can use the local FE space $S_h(T)$ defined on each element $T\in\mathscr{T}_h$, either a non-interface element or an interface element, to define a FE space $S_h(\tilde{\Omega})$ over the whole domain $\tilde{\Omega}$. Since the mesh $\mathscr{T}_h$ used here allows the interface to immerse inside some of its elements, we call $S_h(\tilde{\Omega})$ an IFE space. As pointed out in Reference [11], the IFE space $S_h(\tilde{\Omega})$ is very similar to the standard

FE space based on linear polynomials. For example, we can see that for the same mesh $\mathscr{T}_h$, the IFE space $S_h(\tilde{\Omega})$ and the standard linear FE space have the same number of nodal basis functions; their nodal basis functions have the same supports. Also, we note that when a mesh $\mathscr{T}_h$ is fine enough, most of its elements are non-interface elements, and most of the nodal basis functions of $S_h(\tilde{\Omega})$ are just the usual linear nodal basis functions except for few nodes in the vicinity of the interface $\tilde{\Gamma}$. We refer the readers to Reference [11] for the approximation capabilities and other important features of this IFE space.

For the weak formulation of the interface problem, without loss of generality, let us just assume that $\partial\tilde{\Omega}_N = \emptyset$ and $g_D = 0$. We introduce the following function spaces:

$$\tilde{H}_0^1(\tilde{\Omega}) = \{u(z,r) \mid u \in C(\tilde{\Omega}),\ \ u|_{\partial\tilde{\Omega}} = 0,\ \ u|_{\Omega} \in H^1(\tilde{\Omega}^s),\ s = +,-\}$$

Then the interface problem can be reduced to the following weak problem: find $\tilde{\Phi} \in \tilde{H}_0^1(\tilde{\Omega})$ such that

$$a(v,\tilde{\Phi}) = \langle v, rf\rangle \quad \forall v \in \tilde{H}_0^1(\tilde{\Omega}) \tag{12}$$

where $\langle\cdot,\cdot\rangle$ denotes the standard $L^2(\tilde{\Omega})$ inner product, and the bilinear form $a(\cdot,\cdot)$ is defined as follows:

$$a(v,u) = \int_{\tilde{\Omega}} r\beta\left(\frac{\partial v}{\partial r}\frac{\partial u}{\partial r} + \frac{\partial v}{\partial z}\frac{\partial u}{\partial z}\right) \mathrm{d}r\,\mathrm{d}z \tag{13}$$

Of course, this weak form can also be derived from the 3-D interface problem with the cylindrical transformation.

Then, the weak formulation (12) can be used to form the following IFE equation: find $\tilde{\Phi}_h \in S_{h,0}(\tilde{\Omega})$ such that

$$\sum_{T\in\mathscr{T}_h}\int_T r\beta\left(\frac{\partial v}{\partial r}\frac{\partial\tilde{\Phi}_h}{\partial r} + \frac{\partial v}{\partial z}\frac{\partial\tilde{\Phi}_h}{\partial z}\right)\mathrm{d}r\,\mathrm{d}z = \langle v, rf\rangle \quad \forall v \in S_{h,0}(\tilde{\Omega}) \tag{14}$$

where

$$S_{h,0}(\tilde{\Omega}) = \{u \in S_h(\tilde{\Omega}) \mid u|_{\partial\tilde{\Omega}} = 0\}$$

Note that a discretized bilinear form instead of $a(\cdot,\cdot)$ itself is used in the IFE method above because of the fact that $S_h(\tilde{\Omega}) \not\subset H^1(\tilde{\Omega})$. We call the FE method above the IFE method because of the IFE space used here.

3. A 3-D IFE METHOD

We now consider the general 3-D interface problem (1)–(5). Again we want to develop a suitable FE space that can use structured meshes to solve this kind of interface problems. Without loss of generality, we consider a Cartesian mesh $\mathscr{T}_h$ of the solution domain Ω that is formed by first partitioning Ω into cubes whose edges are parallel to co-ordinate axes, and $\mathscr{T}_h$ is formed by further partitioning each cube into five tetrahedrons in the usual way such that the vertices of each tetrahedron in $\mathscr{T}_h$ are nodes forming those cubes, see Figure 3. The IFE

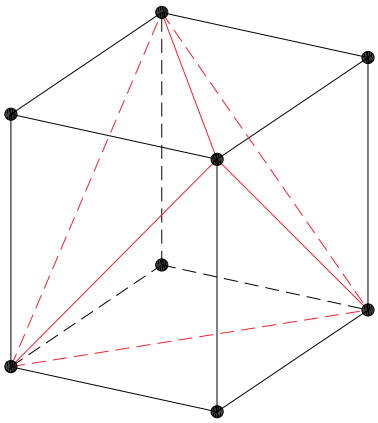

Figure 3. Partitioning of a cubic Cartesian element into five tetrahedrons.

method based on a quadrangular prism mesh using tri-linear basis functions is investigated in our next research project.

Since the mesh $\mathscr{T}_h$ is formed independent of the interface surface Γ, some of the tetrahedrons will intersect with Γ, but most of the elements will not when the mesh is fined enough. Again we call a tetrahedron intersecting with Γ an interface element; otherwise, we call this tetrahedron a non-interface element.

In a typical non-interface element $T \in \mathscr{T}_h$, we use the standard linear local nodal FE basis functions to carry out the approximation. Assume that A_1, A_2, A_3, and A_4 are the four vertices of the tetrahedral element T. We use $\phi_i(\mathbf{x}), i = 1, 2, 3, 4$ to denote those standard linear basis functions such that

$$\phi_i(A_j) = \begin{cases} 1 & \text{if } i = j, \\ 0 & \text{if } i \neq j, \end{cases} \qquad j = 1, 2, 3, 4$$

The local FE space in T is then defined by

$$S_h(T) = \text{span}\{\phi_i(x), i = 1, 2, 3, 4\}$$

Our main effort in this section is to develop the local FE space $S_h(T)$ for each of the interface element $T \in \mathscr{T}_h$ such that each function in this local space will satisfy the interface jump conditions in a certain approximation sense. These local basis functions will be used to form the FE space over the whole solution domain which will be further used to form the IFE method for our interface problem.

3.1. Intersection topology

Investigating the possible intersection topologies between a typical interface tetrahedral element $T \in \mathscr{T}_h$ and the interface surface Γ, we find that it is necessary to consider only two types

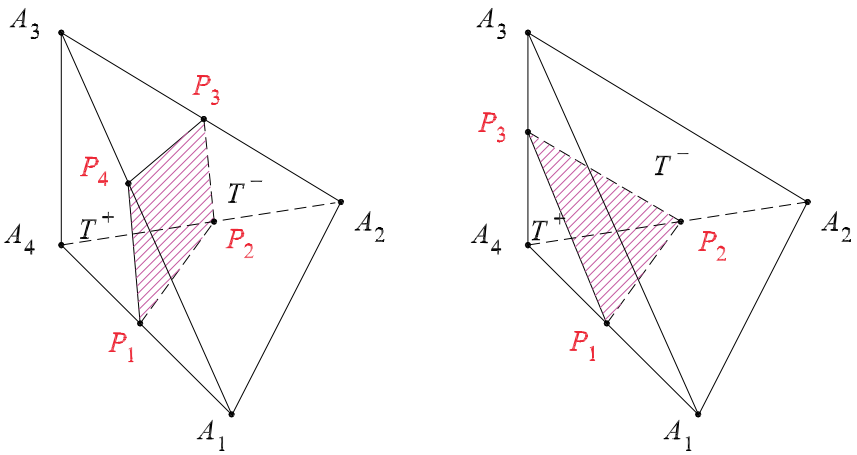

Figure 4. Intersection topologies of tetrahedral elements.

of interface elements, assuming that the mesh size is small enough compared to the interface surface curvature, the rest of the interface elements can be effectively considered as non-interface elements. These two typical intersection topologies are (see Figure 4)

1. *Four-edge cut*: The interface surface Γ intersect with the edges of T at four distinct points on four different edges, and each three of these intersection points are not on a line.
2. *Three-edge cut*: The interface surface Γ intersect with the edges of T at three distinct points which are not on the same face of T.

Other intersection topologies are certainly possible. One possible case is that the interface element T is separated by the interface Γ into three or more sub-regions, each of which has a volume comparable to the others. This generally indicates that the mesh is not fine enough in the neighbourhood of T, and a finer mesh is necessary. Another possibility is that the six edges of the tetrahedron are intersected by a smooth enough surface, like the surface of a sphere with a large enough radius compared to the mesh size. Some edges might even be intersected more than once, see Figure 5. In such a case, we notice that since the surface is smooth, each cut divides the tetrahedron into two sub-regions: a very small sub-region whose volume is nearly zero, and a larger sub-region which nearly occupies the whole tetrahedron. For such case, we can neglect the effect from the sub-regions which have a much smaller volume and assume the tetrahedron is fully occupied by the larger sub-region. In other words, we can just consider the tetrahedron as a non-interface tetrahedron, sitting on one side of the interface. Other situations may be treated similarly.

3.2. IFE local nodal linear basis functions

For a typical interface tetrahedron T with vertices A_i, $(i = 1, 2, 3, 4)$, the interface Γ divides T into two sub-elements into $T^+ = T \cap \Omega^+$ and $T^- = T \cap \Omega^-$. With this natural partition of T,

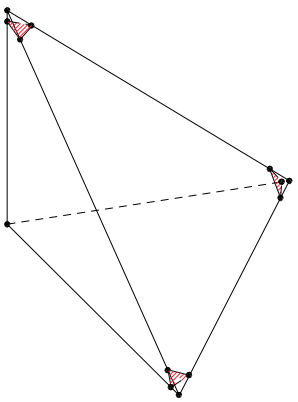

Figure 5. Special intersection topology.

we can introduce four piecewise linear local nodal function $\psi_i(x, y, z), i = 1, 2, 3, 4$

$$\psi_i(\mathbf{x}) = \begin{cases} \psi_i^+(\mathbf{x}) = b_1 x + b_2 y + b_3 z + b_4, & \mathbf{x} \in T^+ \\ \psi_i^-(\mathbf{x}) = b_5 x + b_6 y + b_7 z + b_8, & \mathbf{x} \in T^- \end{cases}$$

that can satisfy the following constraints:

- Nodal values specification:

$$\psi_i(\boldsymbol{A_j}) = \begin{cases} 1, & i = j \\ 0, & i \neq j \end{cases} \qquad i, j = 1, 2, 3, 4$$

- The continuity across the interface inside the tetrahedron $\Gamma_T = T \cap \Gamma$:

$$\psi_i^+(P_j) = \psi_i^-(P_j) \quad i = 1, 2, 3, 4 \quad \text{and} \quad j = 1, 2, 3$$

  Here P_j, $j = 1, 2, 3$ are three points on Γ_T whose choice will be made clear later according to the involved topology of Γ_T.
- The flux continuity across $\tilde{\Gamma}_T$:

$$\int_{\tilde{\Gamma}_T} \left(\beta^+ \frac{\partial \psi_i^+}{\partial \mathbf{n}} - \beta^- \frac{\partial \psi_i^-}{\partial \mathbf{n}} \right) \mathrm{d}s = 0 \quad i = 1, 2, 3, 4$$

  Here $\tilde{\Gamma}_T$ is the plane determined by P_j, $j = 1, 2, 3$ above, and $\mathbf{n}$ is the normal of $\tilde{\Gamma}_T$.

These constraints provide a system of eight simultaneous linear algebraic equations about the coefficients. To show that these conditions are enough to precisely determine a local nodal basis function, we will carry out the discussion in the usual way by transferring the interface element T to the reference tetrahedron $\hat{T}$ with the following affine transformation:

$$\mathbf{x} = A_4 + \mathbf{B} \cdot \mathbf{r} \tag{15}$$

where the vertices of the reference tetrahedron $\hat{T}$ are $\hat{A}_1=(1,0,0)^{\mathrm{T}}$, $\hat{A}_2=(0,1,0)^{\mathrm{T}}$, $\hat{A}_3=(0,0,1)^{\mathrm{T}}$ and $\hat{A}_4=(0,0,0)^{\mathrm{T}}$, $\mathbf{x}=[x,y,z]^{\mathrm{T}}$ is the co-ordinate of a point in the interface element T, and $\mathbf{r}=[r,s,t]^{\mathrm{T}}$ is the co-ordinate of its corresponding point in the reference tetrahedron, and the transformation matrix $\mathbf{B}$ is given by

$$\mathbf{B}=\begin{pmatrix} x_1-x_4 & x_2-x_4 & x_3-x_4 \\ y_1-y_4 & y_2-y_4 & y_3-y_4 \\ z_1-z_4 & z_2-z_4 & z_3-z_4 \end{pmatrix}$$

In reference co-ordinates, the local nodal basis functions have the following expressions:

$$\psi_i(\mathbf{x})=\psi_i(A_4+\mathbf{B}\cdot\mathbf{r})=\hat{\psi}_i(\mathbf{r})=\begin{cases}\hat{\psi}_i^{+}(\mathbf{r})=a_{i,1}r+a_{i,2}s+a_{i,3}t+a_{i,4}, & \mathbf{r}\in T^{+}\\ \hat{\psi}_i^{-}(\mathbf{r})=a_{i,5}r+a_{i,6}s+a_{i,7}t+a_{i,8}, & \mathbf{r}\in T^{-}\end{cases}$$

$$i=1,2,3,4 \tag{16}$$

Then, we plan to show that the nodal value specifications and the interface jump conditions will uniquely determine $\hat{\psi}_i(\mathbf{r})$, $i=1,2,3,4$ and the same conclusion follows for the local nodal basis functions $\psi_i(\mathbf{x})$, $i=1,2,3,4$. To be specific, we need to discuss the two intersection topologies separately.

We first consider the three-edge cut case in which we assume that the interface Γ intersects the edges of an interface element T at three points P_1, P_2 and P_3, see Figure 6. Depending on which edges the interface Γ passes through, there are four possible three-edge cut, two of which are plotted in Figure 6. We will discuss these two cases, and the arguments for the second case apply to the rest.

Assume that the images of P_1, P_2, P_3 in the reference element $\hat{T}$ under the affine mapping are $\hat{P}_1$, $\hat{P}_2$ and $\hat{P}_3$, with the following co-ordinates:

Three-edge cut case 1:

$$\hat{P}_1=[\xi,0,0]^{\mathrm{T}},\quad \hat{P}_2=[0,\eta,0]^{\mathrm{T}},\quad \hat{P}_3=[0,0,\zeta]^{\mathrm{T}} \tag{17}$$

Three-edge cut case 2:

$$\hat{P}_1=[\xi,0,0]^{\mathrm{T}},\quad \hat{P}_2=[1-\eta,\eta,0]^{\mathrm{T}},\quad \hat{P}_3=[1-\zeta,0,\zeta]^{\mathrm{T}} \tag{18}$$

with

$$0\leqslant\xi\leqslant 1,\quad 0\leqslant\eta\leqslant 1,\quad 0\leqslant\zeta\leqslant 1 \tag{19}$$

For three-edge cut case 1, the nodal value specifications lead to the following equations:

$$a_{i,4}=\hat{\psi}_i(\hat{A}_4)=\psi_i(A_4)$$

$$a_{i,5}+a_{i,8}=\hat{\psi}_i(\hat{A}_1)=\psi_i(A_1)$$

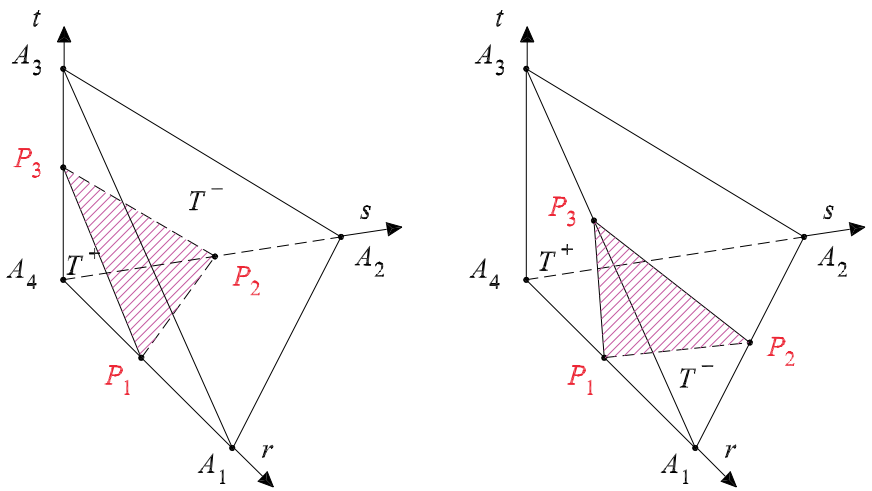

Figure 6. Two cases of possible three-edge cut in the reference element $\hat{T}$.

$$a_{i,6} + a_{i,8} = \hat{\psi}_i(\hat{A}_2) = \psi_i(A_2)$$

$$a_{i,7} + a_{i,8} = \hat{\psi}_i(\hat{A}_3) = \psi_i(A_3)$$

The continuity jump condition across the interface leads to

$$\xi a_{i,1} + a_{i,4} = \xi a_{i,5} + a_{i,8}$$

$$\eta a_{i,2} + a_{i,4} = \eta a_{i,6} + a_{i,8}$$

$$\zeta a_{i,3} + a_{i,4} = \zeta a_{i,7} + a_{i,8}$$

As for the flux continuity condition, we first note that normal $\mathbf{n} = (n_1, n_2, n_3)^{\mathrm{T}}$ is mapped to the vector $\hat{\mathbf{n}} = B^{-1}\mathbf{n} = (\hat{n}_1, \hat{n}_2, \hat{n}_3)^{\mathrm{T}}$ in the reference co-ordinate system. By direct calculation, we can see that the flux continuity condition reduces to

$$\beta^+ \frac{\partial \hat{\psi}_i^+}{\partial \hat{\mathbf{n}}} - \beta^- \frac{\partial \hat{\psi}_i^-}{\partial \hat{\mathbf{n}}} = 0$$

and this leads to

$$(\hat{n}_1 a_{i,1} + \hat{n}_2 a_{i,2} + \hat{n}_3 a_{i,3})\beta^+ = (\hat{n}_1 a_{i,5} + \hat{n}_2 a_{i,6} + \hat{n}_3 a_{i,7})\beta^-$$

Solving these eight linear equations above, we obtain the following formulas about the coefficients:

$$a_{i,1} = \frac{\xi\psi_i(A_1) - \psi_i(A_4) + (1-\xi)a_{i,8}}{\xi}$$

$$a_{i,2} = \frac{\eta\psi_i(A_2) - \psi_i(A_4) + (1-\eta)a_{i,8}}{\eta}$$

$$a_{i,3} = \frac{\zeta\psi_i(A_3) - \psi_i(A_4) + (1-\zeta)a_{i,8}}{\zeta}$$

$$a_{i,4} = \psi_i(A_4)$$

$$a_{i,5} = \psi_i(A_1) - a_{i,8}$$

$$a_{i,6} = \psi_i(A_2) - a_{i,8}$$

$$a_{i,7} = \psi_i(A_3) - a_{i,8}$$

$$a_{i,8} = \frac{\lambda_{i,1}\beta^- + \lambda_{i,2}\beta^+}{\lambda_3\beta^- + \lambda_4\beta^+}$$

where

$$\lambda_{i,1} = \xi\eta\zeta[\hat{n}_1\psi_i(A_1) + \hat{n}_2\psi_i(A_2) + \hat{n}_3\psi_i(A_3)]$$

$$\lambda_{i,2} = \psi_i(A_4)(\hat{n}_1\eta\zeta + \hat{n}_2\zeta\xi + \hat{n}_3\xi\eta) - \lambda_{i,1}$$

$$\lambda_3 = \xi\eta\zeta(\hat{n}_1 + \hat{n}_2 + \hat{n}_3)$$

$$\lambda_4 = \hat{n}_1\eta\zeta + \hat{n}_2\zeta\xi + \hat{n}_3\xi\eta - \lambda_3$$

For the three-edge cut case 2, the nodal value specifications lead to the following equations:

$$a_{i,4} = \hat{\psi}_i(\hat{A}_4) = \psi_i(A_4)$$

$$a_{i,5} + a_{i,8} = \hat{\psi}_i(\hat{A}_1) = \psi_i(A_1)$$

$$a_{i,2} + a_{i,4} = \hat{\psi}_i(\hat{A}_2) = \psi_i(A_2)$$

$$a_{i,3} + a_{i,4} = \hat{\psi}_i(\hat{A}_3) = \psi_i(A_3)$$

The continuity jump condition across the interface leads to

$$\xi a_{i,1} + a_{i,4} = \xi a_{i,5} + a_{i,8}$$

$$(1-\eta)a_{i,1} + \eta a_{i,2} + a_{i,4} = (1-\eta)a_{i,5} + \eta a_{i,6} + a_{i,8}$$

$$(1-\zeta)a_{i,1} + \zeta a_{i,3} + a_{i,4} = (1-\zeta)a_{i,5} + \zeta a_{i,7} + a_{i,8}$$

The flux continuity leads to

$$(\hat{n}_1 a_{i,1} + \hat{n}_2 a_{i,2} + \hat{n}_3 a_{i,3})\beta^+ = (\hat{n}_1 a_{i,5} + \hat{n}_2 a_{i,6} + \hat{n}_3 a_{i,7})\beta^-$$

Solving these eight linear equations above, we obtain the following formulas about the coefficients:

$$
\begin{aligned}
a_{i,1} &= \frac{\xi\psi_i(A_1) - \psi_i(A_4) + (1-\xi)a_{i,8}}{\xi} \\
a_{i,2} &= \psi_i(A_2) - \psi_i(A_4) \\
a_{i,3} &= \psi_i(A_3) - \psi_i(A_4) \\
a_{i,4} &= \psi_i(A_4) \\
a_{i,5} &= \psi_i(A_1) - a_{i,8} \\
a_{i,6} &= \frac{\psi_i(A_2)\eta\xi + \psi_i(A_4)[-1+\eta+\xi(1-\eta)] + a_{i,8}(1-\eta-\xi)}{\eta\xi} \\
a_{i,7} &= \frac{\psi_i(A_3)\zeta\xi + \psi_i(A_4)[-1+\zeta+\xi(1-\zeta)] + a_{i,8}(1-\zeta-\xi)}{\zeta\xi} \\
a_{i,8} &= \frac{\lambda_{i,1}\beta^- + \lambda_{i,2}\beta^+}{\lambda_3\beta^- + \lambda_4\beta^+}
\end{aligned}
$$

where

$$
\begin{aligned}
\lambda_{i,1} &= \xi\eta\zeta\left[\hat{n}_1\psi_i(A_1) + \hat{n}_2\psi_i(A_2) + \hat{n}_3\psi_i(A_3)\right] - \psi_i(A_4)(1-\xi)\left[\hat{n}_2\zeta(1-\eta) + \hat{n}_3\eta(1-\zeta)\right] \\
\lambda_{i,2} &= \eta\zeta\psi_i(A_4)\left[\hat{n}_1 + \xi(\hat{n}_2+\hat{n}_3)\right] - \xi\eta\zeta\left[\hat{n}_1\psi_i(A_1) + \hat{n}_2\psi_i(A_2) + \hat{n}_3\psi_i(A_3)\right] \\
\lambda_3 &= \hat{n}_1\xi\eta\zeta + \hat{n}_2\zeta(-1+\eta+\xi) + \hat{n}_3\eta(-1+\zeta+\xi) \\
\lambda_4 &= \hat{n}_1\eta\zeta(1-\xi)
\end{aligned}
$$

Formulas for the coefficients of the $\hat{\psi}$ in other two cases are similar to those of case 2.

We now turn to the cases for four-edge cut elements. There are three possible four-edge cut elements, one of them is plotted in Figure 7. We will discuss only this type of four-edge cut elements since the construction procedure for its IFE local nodal basis function and the discussion on their properties can be readily applied to any of the other types of four-edge cut elements.

In a four-edge cut interface element T, the four intersection points $P_i, i = 1, 2, 3, 4$ may not, in general, belong to the same plane. So, in order to apply the flux continuity condition, we replace the physical interface surface $\Gamma \cap T$ inside the interface tetrahedron by a plane that is a good approximation of $\Gamma \cap T$. Many procedures may be used to choose such an approximating plane. For example, one can neglect the intersection point that has the minimum normal distance from the plane made by the remaining three intersection points, and let $\tilde{\Gamma}_T$ be the plane spanned by these remaining points. As usual, $\tilde{\Gamma}_T$ is an $O(h^2)$ or better approximation

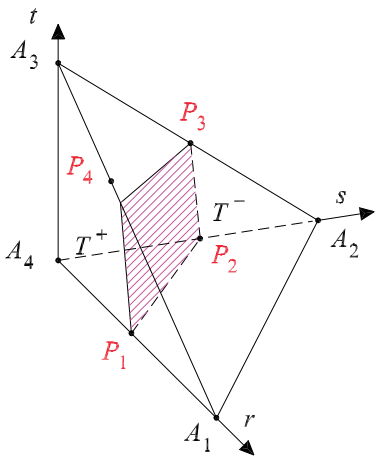

Figure 7. One of the three possible four-edge cut elements in the reference element $\hat{T}$.

to $\Gamma \cap T$ provided that $\Gamma \cap T$ is smooth enough. To be specific, we assume that P_4 is the point to be eliminated, and $\tilde{\Gamma}_T$ is spanned by P_1, P_2 and P_3, see illustration in Figure 7. In this configuration, P_4 is not on $\tilde{\Gamma}_T$. As before, we use transformation (15) to map T to the reference element $\hat{T}$ such that the images of P_1, P_2 and P_3 are

$$\hat{P}_1 = [\xi, 0, 0]^{\mathrm{T}}, \quad \hat{P}_2 = [0, \eta, 0]^{\mathrm{T}}, \quad \hat{P}_3 = [0, 1-\zeta, \zeta]^{\mathrm{T}} \tag{20}$$

We need only to construct the basis functions in the reference element whose formula is given by (16). Then the local nodal IFE basis functions on T is constructed by applying the nodal value specifications and the interface jump conditions as follows.

The nodal value specifications at the vertices:

$$\begin{aligned} a_{i,5} + a_{i,8} &= \psi_i(A_1) \\ a_{i,6} + a_{i,8} &= \psi_i(A_2) \\ a_{i,3} + a_{i,4} &= \psi_i(A_3) \\ a_{i,4} &= \psi_i(A_4) \end{aligned}$$

The continuity at P_1, P_2 and P_3:

$$\begin{aligned} \xi a_{i,1} + a_{i,4} &= \xi a_{i,5} + a_{i,8} \\ \eta a_{i,2} + a_{i,4} &= \eta a_{i,3} + a_{i,8} \\ (1-\zeta) a_{i,2} + \zeta a_{i,3} + a_{i,4} &= (1-\zeta) a_{i,6} + \zeta a_{i,7} + a_{i,8} \end{aligned}$$

The continuity of the flux across the approximate interface $\tilde{\Gamma}_T$:

$$(a_{i,5}\hat{n}_1 + a_{i,6}\hat{n}_2 + a_{i,7}\hat{n}_3)\beta^- = (a_{i,1}\hat{n}_1 + a_{i,2}\hat{n}_2 + a_{i,3}\hat{n}_3)\beta^+$$

These equations lead to the following formulas for coefficients of $\psi_i(\mathbf{r})$:

$$a_{i,1} = \frac{\xi\psi_i(A_1) - \psi_i(A_4) + (1-\xi)a_8}{\xi}$$

$$a_{i,2} = \frac{\eta\psi_i(A_2) - \psi_i(A_4) + (1-\eta)a_8}{\eta}$$

$$a_{i,3} = \psi_i(A_3) - \psi_i(A_4)$$

$$a_{i,4} = \psi_i(A_4)$$

$$a_{i,5} = \psi_i(A_1) - a_{i,8}$$

$$a_{i,6} = \psi_i(A_2) - a_{i,8}$$

$$a_{i,7} = \frac{\eta\zeta\psi_i(A_3) - (1-\eta)(1-\zeta)\psi_i(A_4) + (1-\eta-\zeta)a_{i,8}}{\eta\zeta}$$

$$a_{i,8} = \frac{\lambda_{i,1}\beta^- + \lambda_{i,2}\beta^+}{\lambda_3\beta^- + \lambda_4\beta^+}$$

with

$$\lambda_{i,1} = \xi\eta\zeta\left[\hat{n}_1\psi_i(A_1) + \hat{n}_2\psi_i(A_2) + \hat{n}_3\psi_i(A_3)\right] - \hat{n}_3\xi(1-\eta)(1-\zeta)\psi_i(A_4)$$

$$\lambda_{i,2} = \zeta\left[\hat{n}_1\eta + (\hat{n}_2 + \hat{n}_3\eta)\xi\right]\psi_i(A_4) - \xi\eta\zeta\left[\hat{n}_1\psi_i(A_1) + \hat{n}_2\psi_i(A_2) + \hat{n}_3\psi_i(A_3)\right]$$

$$\lambda_3 = (\hat{n}_1 + \hat{n}_2)\xi\eta\zeta + \hat{n}_3\xi(-1+\eta+\zeta)$$

$$\lambda_4 = \hat{n}_1\eta\zeta(1-\xi) + \hat{n}_2\xi\zeta(1-\eta)$$

Then we can easily prove the following theorem about the existence and uniqueness of the local nodal basis functions.

Theorem 3.1
Assume that T is an interface element such that

$$\lambda_3\beta^- + \lambda_4\beta^+ \neq 0 \tag{21}$$

then the local nodal basis functions defined above in this interface element are uniquely determined by the nodal value specifications and the interface jump conditions.

The assumption in this theorem is true in many situations. For example, this is always true when vertex A_4 of T is one corner of the cube to which T belongs. In fact, in this situation, $\hat{\mathbf{n}}$ is the same as the normal of the plane passing the points $\hat{P}_1$, $\hat{P}_2$ and $\hat{P}_3$. For the first case of a three-edge cut interface element, we know that $\hat{\mathbf{n}} = (\hat{n}_1, \hat{n}_2, \hat{n}_3)^{\mathrm{T}}$ is parallel to $(\xi\zeta, \eta\zeta, \eta\xi)^{\mathrm{T}}$

and further we have

$$\lambda_3 = \eta(\xi\zeta)^2 + \xi(\eta\zeta)^2 + \zeta(\eta\xi)^2 \tag{22}$$

$$\lambda_4 = (1-\eta)(\xi\zeta)^2 + (1-\xi)(\eta\zeta)^2 + (1-\zeta)(\eta\xi)^2 \tag{23}$$

If (21) is not true, then we must have

$$(\xi\zeta)^2(\eta\beta^- + (1-\eta)\beta^+) = 0$$

$$(\eta\zeta)^2(\xi\beta^- + (1-\xi)\beta^+) = 0$$

$$(\eta\xi)^2(\zeta\beta^- + (1-\zeta)\beta^+) = 0$$

All of these together imply that at least two of the three variables η, ξ and ζ must be zero which is not allowed by the three-edge cut definition.

For the second case of a three-edge cut interface element, we note that $\hat{\mathbf{n}} = (\hat{n}_1, \hat{n}_2, \hat{n}_3)^{\mathrm{T}}$ is parallel to $(\eta\zeta, \zeta(-1+\eta+\xi), \eta(-1+\zeta+\xi))^{\mathrm{T}}$ and further we have

$$\begin{aligned} \lambda_3 &= \xi(\eta\zeta)^2 + \zeta^2(-1+\eta+\xi)^2 + \eta^2(-1+\zeta+\xi)^2 \\ \lambda_4 &= (\eta\zeta)^2(1-\xi) \end{aligned} \tag{24}$$

If (21) is not true, then we must have

$$(\eta\zeta)^2[\xi\beta^- + (1-\xi)\beta^+] = 0$$

$$\zeta^2(-1+\eta+\xi)^2\beta^- = 0$$

$$\eta^2(-1+\zeta+\xi)^2\beta^- = 0$$

All of these together will force $\hat{P}_1$, $\hat{P}_2$ and $\hat{P}_3$ to be on the same face of $\hat{T}$ which implies that P_1, P_2 and P_3 must be on the same face of T contradicting the definition.

Finally, for the four-edge cut configuration considered above, we know that $\hat{\mathbf{n}}$ is parallel to $(\eta\zeta, \zeta\xi, \xi(-1+\eta+\zeta))^{\mathrm{T}}$ and

$$\lambda_3 = (\eta+\xi)\zeta^2\eta + \xi^2(-1+\eta+\zeta)^2$$

$$\lambda_4 = (\eta\zeta)^2(1-\xi) + (\zeta\xi)^2(1-\eta)$$

If (21) is not true, then we must have

$$(\eta+\xi)\zeta^2\eta + \xi^2(-1+\eta+\zeta)^2 = 0$$

$$(\eta\zeta)^2(1-\xi) + (\zeta\xi)^2(1-\eta) = 0$$

and we can easily see that these conditions lead to situations in which either two of P_1, P_2, P_3 are the same or these three points are on a line, contradicting the definition that T is a four-edge cut interface element.

To be specific, we let $\psi_i(\mathbf{x}), i = 1, 2, 3, 4$ be such that

$$\psi_i(A_j) = \begin{cases} 1 & \text{if } i = j \\ 0 & \text{if } i \neq j \end{cases}$$

These local nodal IFE basis functions are closely related with their counterparts for the standard FE space. In particular, we note the two properties stated in the following theorem.

Theorem 3.2
Assume that T is an interface element such that (21) holds, then the local nodal basis functions in this interface element have the following properties:

- Partition of unity:

$$\sum_{i=1}^{4} \psi_i(\mathbf{x}) = 1 \quad \forall \mathbf{x} \in T \tag{25}$$

- These IFE local nodal basis functions are consistent with the standard FE local nodal basis functions in the following sense: if the coefficient β has no discontinuity, i.e. $\beta^- = \beta^+ = \beta$, then

$$\psi_i(\mathbf{x}) = \phi_i(\mathbf{x}), \quad \mathbf{x} \in T \tag{26}$$

Proof
These results can be verified by straightforward algebraic calculations. □

3.3. The 3-D IFE method based on a tetrahedron mesh

As usual, on an interface element $T \in \mathscr{T}_h$, we can introduce a local IFE space

$$S_h(T) = \text{span}\{\psi_i, i = 1, 2, 3, 4\}$$

where $\psi_i(\mathbf{x})$ are local nodal basis functions defined in the previous section. Then, for each node $\mathbf{x}_i$ in the mesh $\mathscr{T}_h$, we introduce a global basis function $\Phi_i(\mathbf{x})$ such that $\Phi_i|_T \in S_h(T)$ for any $T \in \mathscr{T}_h$ and

$$\Phi_i(\mathbf{x}_j) = \begin{cases} 1 & \text{if } i = j \\ 0 & \text{if } i \neq j \end{cases}$$

where $\mathbf{x}_i$ and $\mathbf{x}_j$ are nodes of the mesh $\mathscr{T}_h$. Finally, the IFE space on the whole domain Ω is defined as follows:

$$S_h(\Omega) = \text{span}\{\Phi_i(\mathbf{x}) \mid \mathbf{x}_i \text{ is a node of } \mathscr{T}_h\}$$

We now define our IFE solution to the interface problem (1)–(3) as a function $\Phi_h(\mathbf{x}) = \Phi_h(x, y, z) \in S_h(\Omega)$ such that

$$\sum_{T \in \mathscr{T}_h} \int_T \beta \left(\frac{\partial v}{\partial x}\frac{\partial \Phi_h}{\partial x} + \frac{\partial v}{\partial y}\frac{\partial \Phi_h}{\partial y} + \frac{\partial v}{\partial z}\frac{\partial \Phi_h}{\partial z} \right) \mathrm{d}x\,\mathrm{d}y\,\mathrm{d}z = \langle v, f \rangle \quad \forall v \in S_{h,0}(\Omega)$$

where

$$S_{h,0}(\Omega) = \{u \in S_h(\Omega) \mid u|_{\partial\Omega_D} = 0\}$$

4. NUMERICAL EXPERIMENTS WITH IFE METHODS

In this section, we report some numerical experiments with the IFE methods developed in this article for solving both the axis-symmetrical and the full 3-D interface problems. Cartesian meshes $\mathcal{T}_h$ with mesh size h are used in all of our numerical experiments involving IFE methods, and the interfaces in the numerical example are not trivial. Our numerical experiments indicate that the IFE methods in this paper have the rates of convergence comparable to the standard linear FE method based on body-fit meshes.

The implementation of IFE methods can be done basically in the same way as implementing a standard FE methods with a triangular or tetrahedral mesh via the standard element by element assembling procedure. The main difference is the quadrature on interface elements. In each interface element we need to make sure that the quadrature is carried out according to the interface. To do this, we introduce a simple local quadrature partition based on the interface. In the axis-symmetrical IFE method, an interface element is first partitioned into a sub-triangle and a quadrilateral by the line connecting the interface points, see the illustration in Figure 2. The quadrilateral is further partition into two sub-triangles by connecting a pair of opposite vertices. An integration on this interface element can then be carried out on these three sub-triangles according to the standard quadrature formulas on triangles. We have implemented a similar quadrature procedure for the 3-D IFE method, where the quadrature on an interface element is carried out through sub-tetrahedrons instead of sub-triangles, see the illustration in Figure 8.

4.1. An axis-symmetrical interface problem

In this example, we assume that the interface problem has a solution domain that corresponds to the following domain in the z–r plane:

$$\tilde{\Omega} = (0, 1.2) \times (0, 1) \subset \mathbb{R}^2$$

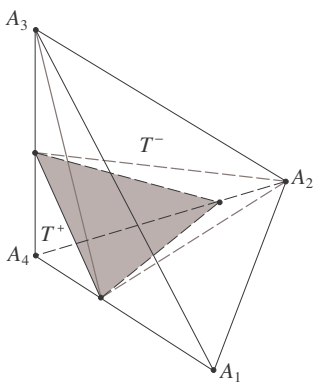

Figure 8. A quadrature partition on an interface tetrahedron.

which is separated into two sub-domains by a circle $\tilde{\Gamma}$ of radius 0.2 centred at $(z, r) = (0.6, 1)$. The part of $\tilde{\Omega}$ inside the circle is $\tilde{\Omega}^-$ and the rest of $\tilde{\Omega}$ is $\tilde{\Omega}^+$. The coefficient is

$$\beta(z, r) = \begin{cases} \beta^- = 1\,000\,000, & (z, r) \in \tilde{\Omega}^- \\ \beta^+ = 1, & (z, r) \in \tilde{\Omega}^+ \end{cases}$$

The boundary conditions used are

$$-\frac{\partial \tilde{\Phi}(z, 0)}{\partial r} = g_{N1}(z), \quad \frac{\partial \tilde{\Phi}(z, 1)}{\partial r} = g_{N2}(z)$$

$$\tilde{\Phi}(0, r) = g_{D1}(r), \quad \tilde{\Phi}(1.2, r) = g_{D2}(r)$$

The functions $f(z, r)$, $g_{N1}(z)$, $g_{N2}(z)$, $g_{D1}(r)$, and $g_{D2}(r)$ are chosen such that the BVP (6)–(8) has the following exact solution:

$$\Phi(z, r) = \begin{cases} \Phi^-(z, r), & (z, r) \in \tilde{\Omega}^- \\ \Phi^+(z, r), & (z, r) \in \tilde{\Omega}^+ \end{cases}$$

$$\Phi^-(z, r) = \frac{1}{\beta^-}((z - 0.6)^2 + (r - 1)^2)^{3/2}$$

$$\Phi^+(z, r) = \frac{1}{\beta^+}((z - 0.6)^2 + (r - 1)^2)^{3/2} + 0.2^3\left(\frac{1}{\beta^-} - \frac{1}{\beta^+}\right)$$

Figure 9 displays a sketch of a typical Cartesian mesh on the solution domain, and Figure 10 displays both the IFE solution $\Phi_h(z, r)$ with $h = 1/96$ and the magnitude of the difference between the IFE solution $\Phi_h(z, r)$ and the exact solution $\tilde{\Phi}(z, r)$.

To find the rate of convergence of the axis-symmetrical IFE method, we carry out numerical simulations with a sequence of Cartesian triangular meshes of decreasing mesh size. The errors in these IFE solutions are measured by the following quantities:

$$E_\infty(h) = \max_i |\Phi(\mathbf{w}_i) - \Phi_h(\mathbf{w}_i)|$$

$$E_0(h) = \|\Phi - \Phi_h\|_0$$

$$E_1(h) = |\Phi - \Phi_h|_1$$

where $\mathbf{w}_i$ is a node of the mesh used to compute $\Phi_h(z, r)$. Numerical quadrature is employed to compute $E_0(h)$ and $E_1(h)$.

The actual error datum are listed in Table I, from which we can see that, when the mesh size is halved, the L^2 norm error is reduced by a factor about 4, and the semi-H^1 error is reduced by a factor about 2. These suggest a second order convergence in L^2 norm, a first

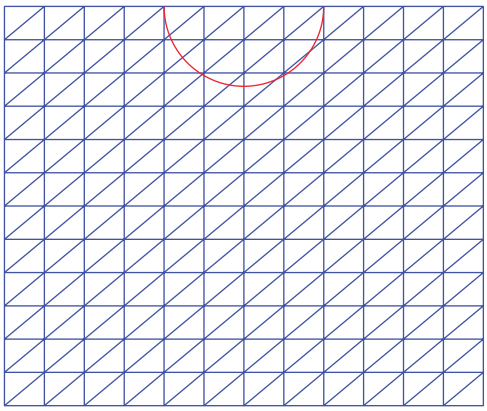

Figure 9. A typical mesh in the solution domain.

order convergence in H^1 norm for the axis-symmetrical IFE method. With these datum and linear regression, we can also see that

$$E_0(h) \approx 0.460h^{1.95}$$

$$E_1(h) \approx 0.889h^{1.02}$$

which further confirms the above observation about the order of convergence for the axis-symmetrical IFE method. We note that orders of convergence are in agreement with approximation capability of the general 2-D IFE space demonstrated in Reference [11].

We also note the following estimate about the rate of convergence in the discrete L^∞ norm:

$$E_\infty(h) = 0.448h^{1.60}$$

which seems to indicate that the axis-symmetrical IFE method does not have a second order convergence in the L^∞ norm. Similar phenomena has also been observed in other IFE method [11].

As mentioned in Section 2, we expect the IFE method to perform well for a spectrum of interfaces whose sizes with respect to the whole domain vary from small to large, so long as the mesh is fine enough to resolve the geometrical properties of these interfaces. For instance, for the particular example presented here, we have carried out a group of simulations in each of which the radius of the interface takes a value from: $\{0.1, 0.2, 0.4, 0.6\}$. In each case, the same sequence of meshes are employed and the IFE method demonstrate convergence rates similar to that reported above.

4.2. Three-dimensional interface examples

4.2.1. An interface problem with a spherical interface. In this example, the interface problem has the following solution domain:

$$\Omega = (-1, 1) \times (-1, 1) \times (-1, 1) \subset \mathbb{R}^3$$

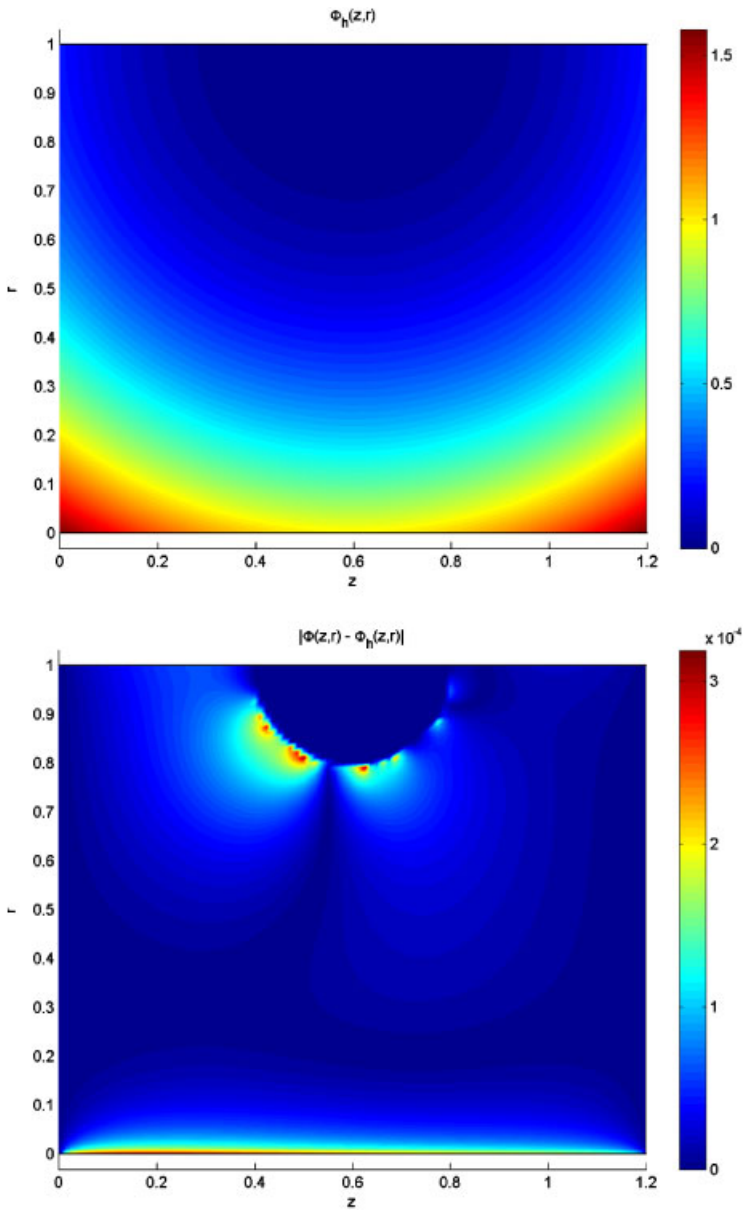

Figure 10. The plot on top is for the IFE solution with $h = 1/96$, and the plot at bottom is for the magnitude of the difference between the IFE solution and the exact solution.

which is separated into two sub-domains by a sphere Γ of radius $r_0 = 11/7\pi$ centred at $(x, y, z) = (0, 0, 0)$. See Figure 11 for a sketch of the solution domain and the interface surface.

Table I. L^2 and semi-H^1 errors of IFE solutions generated with meshes of decreasing mesh size h.

h	$E_0(h)$	$E_1(h)$	$E_\infty(h)$
0.1000000	0.00501159670449	0.08683071871583	0.01276225946915
0.0500000	0.00131688088162	0.04214193918178	0.00436216163085
0.0250000	0.00035176134732	0.02055824762580	0.00113420240666
0.0125000	0.00009035274334	0.01014105825540	0.00031873499405
0.0062500	0.00002407512944	0.00506734734894	0.00013913258660
0.0031250	0.00000622157349	0.00252063662766	0.00005198626863
0.0015625	0.00000144194954	0.00125294481960	0.00001690124205

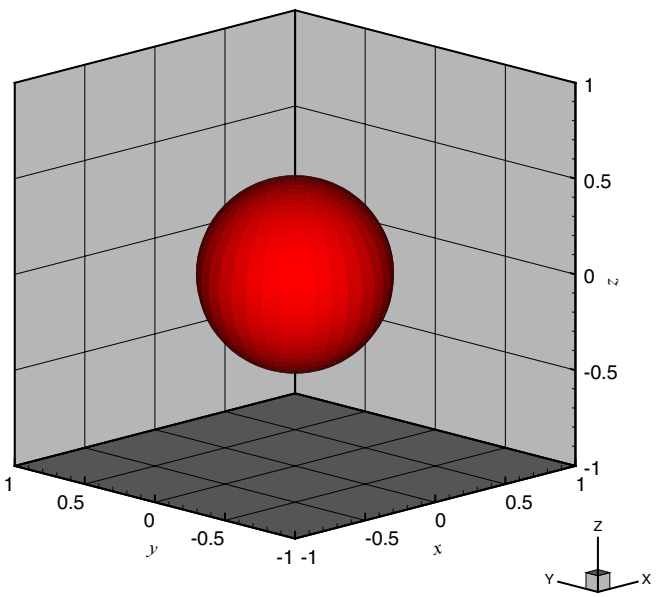

Figure 11. Geometry of the spherical interface problem.

The part of Ω inside the sphere is Ω^+ and the rest of Ω is Ω^-. The coefficient β is a piecewise constant function defined by

$$\beta(\mathbf{x}) = \begin{cases} \beta^+, & r \leqslant r_0 \\ \beta^-, & r > r_0 \end{cases}$$

$$r = \sqrt{x^2 + y^2 + z^2}$$

The boundary conditions used are

$$\Phi(-1, y, z) = g_{D1}(y, z), \quad \Phi(1, y, z) = g_{D2}(y, z)$$

Table II. L^2 and H^1 interpolation errors of IFE functions generated with meshes of decreasing size h and $\beta^+/\beta^- = 10$.

h	$I_0(h)$	$I_1(h)$
1/10	0.02863074709784	0.60886262114381
2/25	0.01832005577936	0.48689457895889
1/15	0.01272535823591	0.40587074291109
1/20	0.00715981392140	0.30451088877053
1/25	0.00458276030469	0.24361267026969
1/30	0.00318292840028	0.20305190742799
1/40	0.00179054795537	0.15229665761824

$$\Phi(x,-1,z) = g_{D2}(x,z), \quad \Phi(x,1,z) = g_{D4}(x,z)$$

$$\Phi(x,y,-1) = g_{D5}(x,y), \quad \Phi(x,y,1) = g_{D6}(x,y)$$

The functions $f, g_{D1}, g_{D2}, g_{D3}, g_{D4}, g_{D5}$, and g_{D6} are chosen such that the BVP (1)–(3) has the following exact solution:

$$\Phi(\mathbf{x}) = \begin{cases} \Phi^-(\mathbf{x}) = \dfrac{1}{\beta^-} r^\alpha, & r \leqslant r_0 \\ \Phi^+(\mathbf{x}) = \dfrac{1}{\beta^+} r^\alpha + \left(\dfrac{1}{\beta^-} - \dfrac{1}{\beta^+} \right) r_0^\alpha, & r > r_0 \end{cases}$$

$$r = \sqrt{x^2 + y^2 + z^2}, \quad \alpha = 3$$

We carried out several numerical experiments using the general 3-D IFE solver with a sequence of Cartesian tetrahedral meshes of decreasing sizes.

First, we investigate the interpolation accuracy of the general 3-D IFE space. For the function $\Phi(\mathbf{x})$ above, we let $I_h\Phi(\mathbf{x}) \in S_h(\Omega)$ be its interpolation. The accuracy of the interpolant is measured with the usual L^2 and semi-H^1 norm:

$$I_0(h) = \|\Phi - I_h\Phi\|_0$$

$$I_1(h) = |\Phi - I_h\Phi|_1$$

We perform two groups of numerical experiments in which β^+ and β^- have two configurations, namely $\beta^+/\beta^- = 10$ and 10 000, respectively. We intend here to prove whether the IFE space has the capability to handle large variations in the material property. The actual error in the interpolants are listed in Tables II and III.

Second, we investigate the accuracy of the 3-D IFE solution $\Phi_h(\mathbf{x})$ for the interface problem by evaluating its error in the L^∞, L^2 and semi-H^1 norms. The numerical experiment is performed using the same configuration in β^+ and β^-, i.e. $\beta^+/\beta^- = 10$ and 10 000, and the results are provided in Tables IV and V.

Table III. L^2 and H^1 interpolation errors of IFE functions generated with meshes of decreasing size h and $\beta^+/\beta^- = 10\,000$.

h	$I_0(h)$	$I_1(h)$
1/10	0.02862398910049	0.60894404495919
2/25	0.01831579080587	0.48689863165034
1/15	0.01272274827558	0.40587259699362
1/20	0.00715869552022	0.30451418926116
1/25	0.00458213262751	0.24360460779908
1/30	0.00318254744428	0.20305086088117
1/40	0.00179036875335	0.15229351567142

Table IV. L^∞, L^2 and H^1 errors of the IFE solutions generated with meshes of decreasing size h and $\beta^+/\beta^- = 10$.

h	$E_\infty(h)$	$E_0(h)$	$E_1(h)$
1/10	0.01262489302636	0.02387342664197	0.49495057794543
2/25	0.00825073841328	0.01517242418900	0.39143251285700
1/15	0.00580847264033	0.01048344761746	0.32350655750840
1/20	0.00332235398796	0.00585709439010	0.24014226078190
1/25	0.00214738110361	0.00373698298722	0.19088595657500
1/30	0.00150096740812	0.00258831338236	0.15843514272363
1/40	0.00092217286665	0.00145268177348	0.11819598247567

Table V. L^∞, L^2 and H^1 errors of the IFE solutions generated with meshes of decreasing size h and $\beta^+/\beta^- = 10\,000$.

h	$E_\infty(h)$	$E_0(h)$	$E_1(h)$
1/10	0.04123830710303	0.04028233863246	0.57321576948048
2/25	0.00828290296566	0.01571469319702	0.39334777132556
1/15	0.00717166170328	0.01166727175801	0.32810277169447
1/20	0.00445179149512	0.00633775025999	0.24167938892083
1/25	0.00304517270175	0.00392699537751	0.19137063572506
1/30	0.00175039148577	0.00272748219896	0.15850300904368
1/40	0.00126436253041	0.00146503903938	0.11780319851313

4.2.2. An interface problem with a hemispherical interface. Now, we examine a similar interface problem, but with the following solution domain:

$$\Omega = (-1, 1) \times (-1, 1) \times (0, 1) \subset \mathbb{R}^3$$

which is separated into two sub-domains by a hemisphere Γ of radius $r_0 = 11/7\pi$ centred at $(x, y, z) = (0, 0, 0)$. In this example, both materials touch the boundary of the solution domain, see Figure 12 for a sketch of the solution domain and interface of this example.

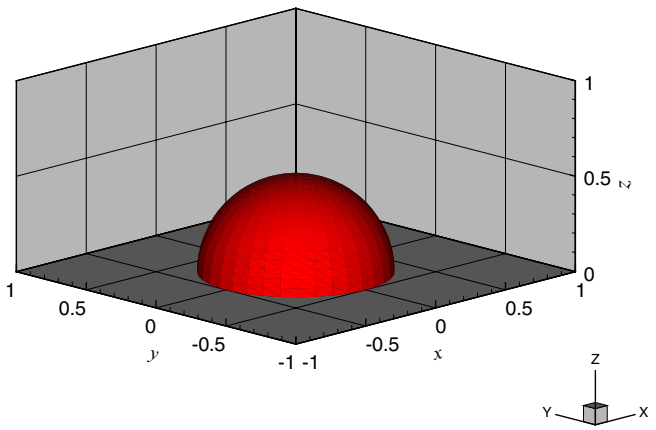

Figure 12. Geometry of the hemispherical interface problem.

The part of Ω inside the hemisphere is Ω^+ and the rest of Ω is Ω^-. The coefficient β is defined the same as in the previous experiment. The boundary conditions used are

$$\Phi(-1, y, z) = g_{D1}(x, y, z), \quad \Phi(1, y, z) = g_{D2}(x, y, z)$$

$$\Phi(x, -1, z) = g_{D2}(x, y, z), \quad \Phi(x, 1, z) = g_{D4}(x, y, z)$$

$$\Phi(x, y, 0) = g_{D5}(x, y, z), \quad \Phi(x, y, 1) = g_{D6}(x, y, z)$$

The functions $f, g_{D1}, g_{D2}, g_{D3}, g_{D4}, g_{D5}$, and g_{D6} are chosen such that the BVP (1)–(3) has the following exact solution:

$$\Phi(\mathbf{x}) = \begin{cases} \Phi^-(\mathbf{x}) = \dfrac{1}{\beta^-} r^\alpha, & r \leqslant r_0 \\ \Phi^+(\mathbf{x}) = \dfrac{1}{\beta^+} r^\alpha + \left(\dfrac{1}{\beta^-} - \dfrac{1}{\beta^+} \right) r_0^\alpha, & r > r_0 \end{cases}$$

$$r = \sqrt{x^2 + y^2 + z^2}$$

The numerical simulations are carried out for this example in a fashion similar to that of the example with a spherical interface reported above, using two configurations in the values of β^+ and β^-, namely $\beta^+/\beta^- = 10$ and 10 000, respectively. The errors in the IFE interpolants and IFE solutions are also evaluated in the same way as above. The IFE interpolation errors are provided in Table VI and Table VII, and the IFE solution errors are provided in Tables VIII and IX.

Applying linear regression on the data in Tables II–IX, we notice that the errors in the IFE interpolants and IFE solutions measured with the usual L^∞, L^2 and semi-H^1 norms for these

Table VI. L^2 and H^1 interpolation errors of IFE functions generated with meshes of decreasing size h and $\beta^+/\beta^- = 10$.

h	$I_0(h)$	$I_1(h)$
1/10	0.01526655291243	0.38077157301392
2/25	0.00976136954738	0.30406200279363
1/15	0.00678042653309	0.25346689687812
1/20	0.00381496195444	0.19015432274360
1/25	0.00244181941472	0.15213094692520
1/30	0.00169589484799	0.12680351542069
1/40	0.00095400761812	0.09509529612487

Table VII. L^2 and H^1 interpolation errors of IFE functions generated with meshes of decreasing size h and $\beta^+/\beta^- = 10\,000$.

h	$I_0(h)$	$I_1(h)$
1/10	0.01526544517406	0.38095359585958
2/25	0.00975932290597	0.30408234793981
1/15	0.00677922839954	0.25347750398174
1/20	0.00381449933577	0.19019885763722
1/25	0.00244151925341	0.15213389179384
1/30	0.00169572332772	0.12681620277591
1/40	0.00095391717509	0.09509558003025

Table VIII. L^∞, L^2 and H^1 errors of the IFE solutions generated with meshes of decreasing size h and $\beta^+/\beta^- = 10$.

h	$E_\infty(h)$	$E_0(h)$	$E_1(h)$
1/10	0.00653992629705	0.01345544182078	0.33596149997161
2/25	0.00426005332010	0.00858970098315	0.26665430426189
1/15	0.00299254262135	0.00596785718525	0.22142076897879
1/20	0.00170715887587	0.00335098172302	0.16528868949120
1/25	0.00144258947210	0.00214061727808	0.13183034247550
1/30	0.00129672652667	0.00149105902063	0.10968845519083
1/40	0.00103930066509	0.00084168504315	0.08210823418007

two 3-D examples obey the following the relation:

$$\text{Error} = ah^b$$

with the parameters a and b listed in Tables X and XI. These regression relations indicate that our general 3-D IFE space has a second order approximation capability in the L^2 norm because of $b \approx 2$, and a first order accuracy in the semi-H^1 norm because of $b \approx 1$. Therefore, the 3-D IFE space developed here seems to have the same approximation capability as the usual linear

Table IX. L^∞, L^2 and H^1 errors of the IFE solutions generated with meshes of decreasing size h and $\beta^+/\beta^- = 10\,000$.

h	$E_\infty(h)$	$E_0(h)$	$E_1(h)$
1/10	0.04916847046074	0.01282708443059	0.35702400379325
2/25	0.01831548599243	0.00820635361076	0.26999051102750
1/15	0.01473116247076	0.00547175116662	0.22462344629681
1/20	0.01022350299275	0.00316224468216	0.16737642560765
1/25	0.00806842216169	0.00210193345367	0.13433075504405
1/30	0.00505398410515	0.00142201969521	0.11085971103636
1/40	0.00254355780247	0.00080910256459	0.08258292175082

Table X. Regression constants of the relation between interpolation error and mesh size.

		L^2 error		H^1 error	
	β^+/β^-	a	b	a	b
Sphere	10	2.86	2.0	6.08	1.0
	10 000	2.86	2.0	6.08	1.0
Hemisphere	10	3.81	2.0	1.53	1.0
	10 000	3.81	2.0	1.52	1.0

Table XI. Regression constants of the relation between IFE solution error and mesh size.

		L^∞ error		L^2 error		H^1 error	
	β^+/β^-	a	b	a	b	a	b
Sphere	10	1.01	1.91	2.49	2.02	5.31	1.03
	10 000	3.8	2.23	5.77	2.26	6.76	1.11
Hemisphere	10	0.12	1.34	1.34	2.0	3.47	1.02
	10 000	2.78	1.87	1.22	1.98	3.81	1.04

FE space based on unstructured body-fitting mesh. However, our numerical experiments with hemispherical example tell us that the 3-D IFE solution to the interface problem cannot always generate a second order approximation in the L^∞ norm because for this example we have $b<2$. Under what conditions the 3-D IFE solution can produce a second order approximation in the L^∞ norm deserves further investigation.

4.3. Application in ion thruster optics simulation

We present here the application of the IFE method in PIC simulations of ion thruster optics. Ion thruster, a type of electric propulsion device, propels a spacecraft by continuously emitting

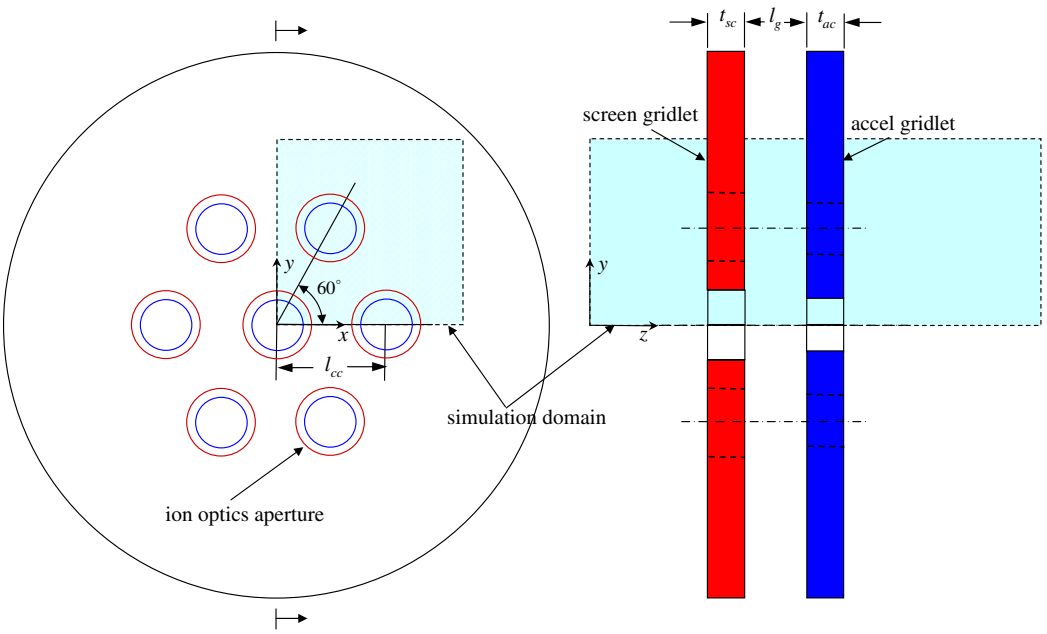

Figure 13. A layout of sub-scale ion optics gridlets.

a high-energy ion beam. The ion optics is the component that accelerates the propellant ions using the electrostatic force. An ion optics typically consists of a screen grid and an accelerator grid, each with many apertures arranged in a hexagonal layout. A high-voltage difference (typically over 1000 V) is applied in between the two grids (typically separated by a distance of a few mm) to focus the ions through the apertures to produce the thrust [22]. Experimental research of ion optics are sometimes performed on a sub-scale gridlet consisting of a sub-set of the apertures.

Recently, a PIC model was developed to simulate a whole sub-scale optics gridlet shown in Figure 13. In this model, the IFE method is applied to solve the electric field in the PIC code. The sub-scale gridlet consists of two 7-aperture conducting grids separated at the edge by a dielectric spacer. The dimensions and physical parameters of the optics gridlet are given in Table XII. The details of the model set-up are discussed in Reference [23]. Here we only show the solution of the electric field at the starting point of the PIC simulation, when no ion particles exist in the simulation domain and the electrons upstream of the screen grid are in a steady, equilibrium state. The electric field is solved from

$$-\nabla \cdot (\beta \nabla \Phi) = n_0 \exp\left(\frac{\Phi - \Phi_0}{T_{e0}}\right)$$

for the domain upstream of the screen grid (where n_0, Φ_0, and T_{e0} are the plasma density, plasma potential, and electron temperature of the upstream discharge plasma, respectively)

Table XII. Nominal dimensions and operating conditions of the NSTAR ion thruster.

Screen hole diameter, d_{sc}	1.91 mm
Screen grid thickness, t_{sc}	0.38 mm
Acceleration hole diameter, d_{ac}	1.14 mm
Acceleration grid thickness, t_{ac}	0.51 mm
Screen to acceleration grid gap, l_g	0.58 mm
Centre-to-centre hole spacing, l_{cc}	2.21 mm
Total accelerating voltage	1100 V
Screen grid voltage	1074 V
Acceleration grid voltage	−180 V

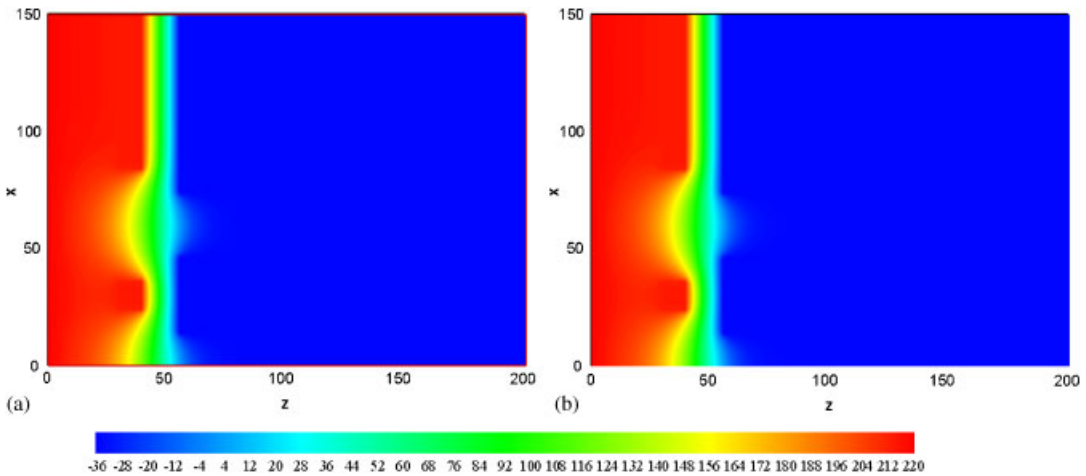

Figure 14. Comparison of IFE and FEM solutions at the horizontal plane of symmetry (note that all potentials are normalized by the upstream electron temperature, $T_{e0} = 5\,\text{eV}$): (a) IFE solution; and (b) FEM solution.

and

$$-\nabla \cdot (\beta \nabla \Phi) = 0$$

for the rest of domain.

For the purpose of comparison and validation, we solve the initial electric field from the above equations using both the IFE method with a Cartesian grid and the standard linear FE using a body-fit tetrahedral mesh. The IFE and FEM solutions at the horizontal plane cutting through both gridlets are shown in Figure 14. Also, the solutions are compared on the mid-plane of the screen gridlet in Figure 15. The Cartesian IFE mesh and unstructured body-fit FE mesh are illustrated in Figure 16 by a 2-D slice cutting through the mid-thickness of the screen

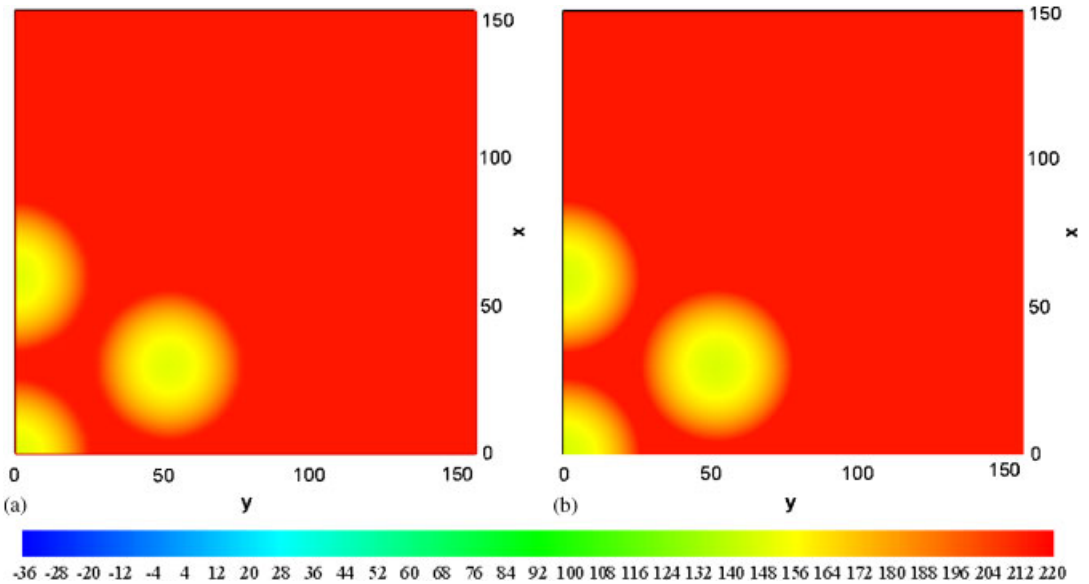

Figure 15. Comparison of IFE and FEM solutions at the mid-plane of the screen gridlet (note that all potentials are normalized by the upstream electron temperature, $T_{e0} = 5\,\text{eV}$): (a) IFE solution; and (b) FEM solution.

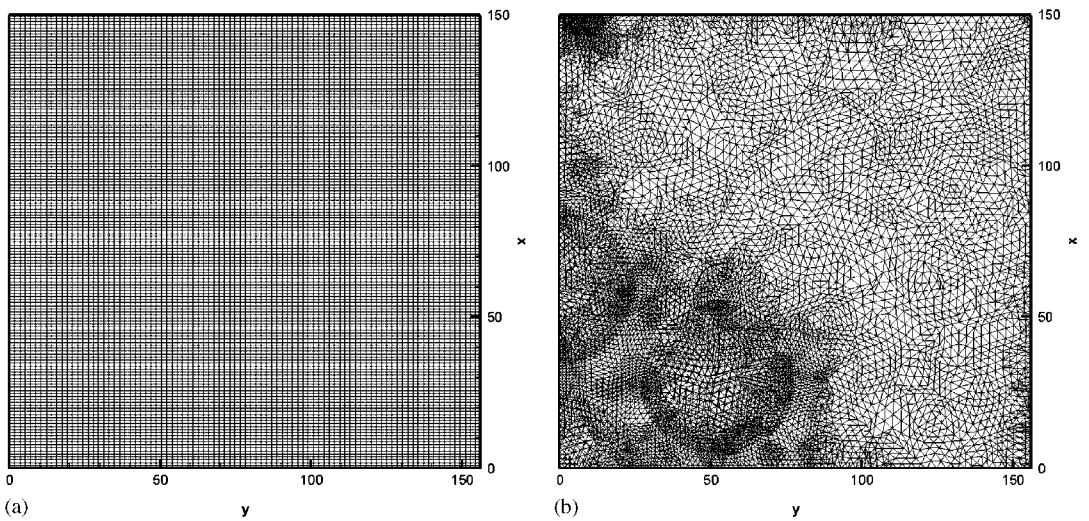

Figure 16. Comparison of IFE and FEM meshes at the mid-plane of the screen gridlet: (a) IFE mesh; and (b) FEM mesh.

gridlet. We find that both the IFE method using a uniform Cartesian mesh the FEM using a body-fit unstructured mesh provide the same results from the point of view of numerical approximations.

5. CONCLUSIONS

In this article, we have developed two immersed finite element (IFE) methods that can use structured Cartesian meshes to compute electric field in a 3-D domain formed by composite materials with non-trivial interfaces. The methods and their main ideas can be applied to other 3-D interface problems involving the second order elliptic partial differential equations. In comparison with the standard finite element (FE) method using linear polynomials, the IFE methods presented here have two major distinctions:

- To maintain the accuracy, the mesh used in the standard FE method has to be formed according to the location of the interface while the mesh of an IFE method is not subject to the constraint of the interface. If preferred, a Cartesian mesh can be used in an IFE method.
- On the other hand, the basis functions in the standard FE method are universally formed independent of the interface and material changes, while some of the basis functions in the IFE method will incorporate the interface location and the interface jump conditions according to the variation in the material property.

We now summarize the main features and benefits of the IFE methods as follows.

1. Structured meshes, in particular a Cartesian mesh, can be used in the IFE method, and this facilitates efficient particle tracking in a PIC code. At the same time, IFE methods developed here have the same approximation capability measured in the usual L^2 and H^1 norms as the standard body-fitting FE method based on linear polynomials.
2. The trial functions in the IFE method satisfy the jump conditions at the interface imposed by material properties. This not only makes the solution accurate numerically but also allows the numerical solution to explicitly maintain the desired physics for across a given material interface.
3. On the other hand, the IFE methods are also closely related to the standard FE method based on linear polynomials. First, the basis functions in the IFE methods reduce to the standard linear basis functions when the material coefficient has no discontinuity. Second, if the same mesh is used, the algebraic systems in both the IFE method and the standard FE method have the same structure because these two methods will have the same number of basis functions and the supports of their basis functions are the same. Also, the programming procedures for both the IFE method and standard FE method are almost identical, and this facilitate quick transformation of the existing codes for the standard FE method to the IFE method.
4. Since the mesh can be generated independently from the material interface in an IFE method, one can use the same mesh to handle a class of interface problems with different interface configurations (so long as the mesh is fine enough according to the geometry of all the interfaces involved). In particular, small changes in interface geometry will not require the use of a new mesh in an IFE method.
5. Because of the FE formulation, the involved algebraic systems in the IFE method are symmetric and positive definite. In contrast to those immerse/imbedded boundary techniques based on finite difference formulation, IFE method achieves this critical feature without sacrificing the accuracy of its approximation capability in the vicinity of the interface.

6. With a Cartesian mesh, the algebraic systems in the IFE method can have the usual desirable banded structure as in some of the immersed/imbedded boundary techniques based on finite difference. This banded structure and the structured mesh in the IFE method allow easy deployment of fast solution techniques such as ADI, preconditioned conjugate gradient, and multi-grid methods.

REFERENCES

1. Birdsall CK, Langdon AB. *Plasma Physics via Computer Simulation*. McGraw-Hill: New York, 1985.
2. Hockney RW, Eastwood JW. *Computer Simulation Using Particles*. McGraw-Hill: New York, 1981.
3. Babuška I. The finite element method for elliptic equations with discontinuous coefficients. *Computing* 1970; **5**:207–213.
4. Chen Z, Zou J. Finite element methods and their convergence for elliptic and parabolic interface problems. *Numeriche Mathematik* 1998; **79**:175–202.
5. Samarskiĭ AA, Andreev VB. *Méthods aux Différences pour Équations Ellipticques*. Mir: Moscow, 1978.
6. Heinrich B. *Finite Difference Methods on Irregular Networks*. International Series of Numerical Mathematics, vol. 82. Birkhäuser: Boston, 1987.
7. Westermann T. Localization schemes in 2d boundary-fitted grids. *Journal of Computational Physics* 1992; **101**:307.
8. Wang J, Kondrashov D, Liewer P, Karmesin S. 3-d deformable grid electromagnetic particle-in-cell for parallel computers. *Journal of Plasma Physics* 1999; **61**(3):367–389.
9. Ewing R, Li Z, Lin T, Lin Y. The immersed finite volume element methods for the elliptic interface problems. *Mathematics and Computers in Simulation* 1999; **50**:63–76.
10. Li Z. The immersed interface method using a finite element formulation. *Applied Numerical Mathematics* 1998; **27**:253–267.
11. Li Z, Lin T, Lin Y, Rogers R. An immersed finite element space and its approximation capability. *Numerical Methods for Partial Differential Equations* 2004; **20**(3):338–367.
12. Li Z, Lin T, Wu X. New Cartesian grid methods for interface problems using finite element formulation. *Numerische Mathematik* 2003; **96**(1):61–98.
13. Lin T, Lin Y, Rogers RC, Ryan LM. A rectangular immersed finite element method for interface problems. In *Advances in Computation*: *Theory and Practice*, vol. 7, Minev P, Lin Y (eds). Nova Science Publishers, Inc.: New York, 2001; 107–114.
14. Zhang L, Gerstenberger A, Wang X, Liu WK. Immersed finite element method. *Computer Methods in Applied Mechanics and Engineering* 2004; **193**:2051–2067.
15. Dadone A, Grossman B. An immersed body methodology for inviscid flows on Cartesian grids. *AIAA 2002-1059*.
16. Hewett DW. The embedded curved boundary method for orthogonal simulation meshes. *Journal of Computational Physics* 1997; **138**:585–616.
17. Babuška I, Melenk J. The partition of unity method. *International Journal for Numerical Methods in Engineering* 1997; **40**:727–758.
18. Babuška I, Osborn JE. Generalized finite element methods: their performance and relation to mixed methods. *SIAM Journal on Numerical Analysis* 1983; **20**(3):510–536.
19. Belytschko T, Moës N, Usui S, Primi C. Arbitrary discontinuities in finite elements. *International Journal for Numerical Methods in Engineering* 2001; **50**:993–1013.
20. Moës N, Dolbow J, Belytschko T. A finite element method for crack growth without remeshing. *International Journal for Numerical Methods in Engineering* 1999; **46**(1):131–150.
21. Sukemar N, Chopp DL, Moës N, Belytschko T. Modeling holes and inclusions by level set in the extended finite-element method. *Computer Methods in Applied Mechanics and Engineering* 2001; **190**:6183–6200.
22. Wang J, Polk J, Brophy J, Katz I. Three-dimensional particle simulation of ion thruster optics blasma flow and grid erosion. *Journal of Propulsion and Power* 2003; **19**(6):1192–1199.
23. Kafafy R, Wang J. Whole ion optics simulations of a subscale gridlet using a hybrid-grid IFE-PIC code. *40th AIAA/ASME/SAE/ASEE Joint Propulsion Conference and Exhibit*, *AIAA 04-3783*, Fort Lauderdale, Florida, July 2004.

